International Journal of Nanomedicine

Dovepress
open access to scientific and medical research

Open Access Full Text Article

ORIGINAL RESEARCH

A Novel pH-Responsive Iron Oxide Core-Shell Magnetic Mesoporous Silica Nanoparticle (M-MSN) System Encapsulating Doxorubicin (DOX) and Glucose Oxidase (Gox) for Pancreatic Cancer Treatment

Guiqiang Qi[1], Guangyue Shi[1], Shengchao Wang[1], Haifeng Hu[2], Zhichen Zhang[1], Qiangqiang Yin[1], Zhongtao Li[1], Liguo Hao[1,3]

[1]Department of Molecular Imaging, School of Medical Technology, Qiqihar Medical University, Qiqihar, Heilongjiang, 161006, People's Republic of China; [2]Medical Imaging Center, The Second Affiliated Hospital of Qiqihar Medical University, Qiqihar, Heilongjiang, 161000, People's Republic of China; [3]Department of Molecular Imaging, The First Affiliated Hospital of Qiqihar Medical University, Qiqihar, Heilongjiang, 161041, People's Republic of China

Correspondence: Liguo Hao, Email haoliguo@qmu.edu.cn

Introduction: This study developed a pancreatic cancer targeted drug delivery system that responds to changes in acidity. The system was based on iron oxide core-shell magnetic mesoporous silica nanoparticles (M-MSNs) to treat pancreatic cancer through combined chemotherapy and starvation therapy.

Methods: Glucose oxidase (Gox) was coupled to the cancer cell surface to reduce glucose availability for cancer cells, exacerbating the heterogeneity of the tumor microenvironment. Reduced pH accelerated the depolymerization of pH-sensitive polydopamine (PDA), thereby controlling the spatial distribution of Gox and release of doxorubicin (DOX) within tumor cells.

Results: Characterization results showed the successful synthesis of DG@M-MSN-PDA-PEG-FA (DG@NPs) with a diameter of 66.02 ± 3.6 nm. In vitro data indicated DG@NPs were highly effective and stable with good cellular uptake shown by confocal laser scanning microscopy (CLSM). DG@NPs exhibited high cytotoxicity and induced apoptosis. Additionally, in vivo experiments confirmed DG@NPs effectively inhibited tumor growth in nude mice with good biosafety. The combination of starvation therapy and chemotherapy facilitated drug release, suggesting DG@NPs as a novel drug delivery system for pancreatic cancer treatment.

Conclusion: This study successfully constructed a doxorubicin release system responsive to acidity changes for targeted delivery in pancreatic cancer, providing a new strategy for combination therapy.

Keywords: mesoporous silica nanoparticle, drug delivery, multitherapy modality, magnetic resonance imaging, glucose oxidase

Introduction

Pancreatic cancer is a deadly malignancy with a five-year survival rate below 10%, and its incidence and mortality are increasing globally.[1,2] The main treatments for pancreatic cancer include surgical resection, radiotherapy and chemotherapy, but the current methods are not ideal due to the characteristics of pancreatic cancer, such as difficulty in early diagnosis, robust tumor invasiveness, fast metastasis, and high multidrug resistance.[2–4] Therefore, developing novel diagnostic and therapeutic strategies for pancreatic cancer is urgently needed. Drug delivery systems (DDSs) have demonstrated significant promise for tumor detection and therapy in recent years.[5,6] DDSs can improve the solubility, stability and biodistribution of drugs and enhance their accumulation in and targeting to tumor tissues, thereby increasing the antitumor effect of the drug and reducing toxic side effects.[5–8] As a result, various functionalized nanocarriers have emerged, such as liposomes, mesoporous silica nanoparticles (MSNs) and metal organic

Received: 20 August 2023
Accepted: 21 November 2023
Published: 30 November 2023

frameworks (MOFs).[9,10] Nanocarriers are also increasingly being studied for drug and gene delivery in other cancers. For example, liposomes are biocompatible and can be used to deliver drugs and miRNAs to silence oncogenes, thereby inhibiting the development of pancreatic cancer.[11–13] Polymeric nanoparticles such as polylactic acid-hydroxy acetic acid copolymers can passively aggregate in tumour tissues through the EPR effect to achieve targeted delivery of drugs.[14] Metallic nanoparticles such as gold nanoparticles can be combined with photothermal conversion compounds to kill cancer cells using the thermal effect of near-infrared light irradiation.[15,16] These representative nanocarriers bring new hope for the treatment of pancreatic cancer and other cancers. However, the problems of low drug loading and low targeting ability also exist, which need to be further optimized to improve the therapeutic efficacy. M-MSNs have drawn attention due to their great pore capacity, tunable pore size, high specific surface area, and superior biosafety. However, their potential clinical applications are limited due to premature drug release and the need for intelligent release of the load.[17–21]

"Gatekeepers" that respond to specific stimuli and intelligently control drug release could significantly improve the therapeutic efficacy of cancer drugs. Polydopamine (PDA) is a biomimetic polymer with good biocompatibility and photothermal conversion properties.[22,23] PDA can release drugs in response to various mechanisms and can regulate the drug release rate according to the characteristics of the tumor microenvironment (pH, enzymes, redox, etc.) and improve the therapeutic efficacy and safety of the drug.[24,25] As a result, PDA has received much attention as a "gatekeeper" in drug release. However, the tumor microenvironment makes achieving rapid drug release difficult, and the resistance of tumors to single drugs limits their therapeutic efficacy. Combining the characteristics of various treatment methods and materials chemistry, a synergistic treatment method that overcomes the disadvantages of monotherapy is proposed here. Doxorubicin (DOX) is a chemical drug widely used clinically with good antitumor activity against various tumor types. Glucose oxidase (Gox) has the ability to disrupt the supply of oxygen and glucose to tumors, thereby altering the pathological environment and enhancing the anticancer effects of chemotherapy drugs. Thus, Gox can be used as a synergistic agent with DOX for starvation-chemotherapy synergistic therapy.[26–29] In addition, folate receptors (FRs) are considered a potential target for cancer therapeutics because they are overexpressed in many cancer cells.[30–33] For example, SW1990 pancreatic cancer cells highly express FRs and could be the subject of research targeting pancreatic cancer.

Hence, we developed a stable shell-core structured drug delivery system for accurate cancer diagnosis and dual-mode therapy. PDA acts as a "gatekeeper" to control the intelligent release of drugs, and folic acid (FA) gives the system the ability to target FRs. In this study, Gox consumed glucose in tumor cells to produce glucuronic acid and H_2O_2, enabling starvation therapy while exacerbating the hypoxic state of the tumor and reducing the metabolism and excretion of DOX, ultimately allowing DOX to exert its antitumor effects more effectively. The H_2O_2 produced by Gox can also induce oxidative stress and apoptosis in tumor cells, enhance the killing effect of DOX, and realizing synergistic pancreatic cancer treatment. In addition, superparamagnetic Fe_3O_4 enhances the T_2-weighted MRI ability of the nanoparticles, thus achieving accurate tumor diagnosis. In summary, this system provides an interesting mode for the accurate diagnosis and effective dual-modal treatment of cancer.

Materials and Methods

Materials

All reagents listed below were of analytical grade and used without further purification. Cetyltrimethylammonium bromide (CTAB), iron (III) acetylacetonate ($Fe(acac)_3$), zinc acetylacetonate ($Zn(acac)_3$), tetraethyl orthosilicate (TEOS), N-hydroxy succinimide (NHS), and N-ethyl-N′-(3-dimethylaminopropyl) carbodiimide (EDC) were purchased from Aladdin Co. (Shanghai, China). An apoptosis assay kit was purchased from KGI Bio (Jiangsu, China).

The cell lines used in this study were obtained from Haixing Biosciences Limited Company. Their procurement and use complied with ethical regulations.

Synthesis of Fe_3O_4 Nanoparticles

First, 1.94 g of $Fe(acac)_3$, 0.22 g of $Zn(acac)_3$, 7.4 g of oleic acid and 1.15 g of sodium oleate were accurately weighed and placed into a 250 mL three-necked flask. Next, 1.1 g of 1-octadecene, 52 mL of benzyl diethyl ether, and 11 g of

1-tetradecene were added. Argon was injected, and the temperature was raised to 300 °C at a rate of 3 °C/min for 1 h. The particles were washed three times with 10 mL of n-hexane, ultrasonicated, and redispersed. The particles were mixed with 10 mL of anhydrous ethanol and centrifuged for 15 min at 10,000 rpm, and the supernatant was discarded. The final product was stored in n-hexane.

Synthesis of M-MSN-NH_2 Nanoparticles

CTAB (1.2 g) was dispersed in 60 mL of deionized water, followed by the addition of 6 mL (5 mg/mL) of well-dispersed Fe_3O_4 nanosolution. The resulting mixture was sonicated at 80 °C for 1 h. The reaction was continued by adding 2.7 mL of TEOS dropwise and heating the mixture at 80 °C for 4 h at 600 rpm. M-MSNs were heated to reflux three times for 6 h in 100 mL of NaCl-methanol solution (1.25 wt.% NaCl) to obtain M-MSNs. Then, 250 mg of M-MSN was mixed with 1.2 mL of APTES, and the mixture was placed in 50 mL of anhydrous toluene to reflux for 24 h. Afterward, the mixture was centrifuged at 12,000 rpm for 15 min to collect M-MSN-NH_2.

Synthesis of DG@M-MSNs

Fifty milligrams of M-MSN-NH_2, 10 mg of DOX, and 10 mL of ultrapure water were weighed into a 25 mL flask, and the mixture was stirred for 24 h to obtain nanoparticles loaded with DOX (DOX@M-MSNs-NH_2). EDC-HCl (80 mg), NHS (120 mg), and Gox (15 mg) were added to a 25 mL flask for 30 min of activation, then 12 mL of deionized water was added, and the mixture stirred for 8 h. Finally, 50 mg of DOX@M-MSNs-NH_2 was added. Then, the reaction was continued on a shaker for 2 h to obtain the product DG@M-MSNs.

Synthesis of DG@NPs

Fifty milligrams of DG@M-MSNs was dispersed in 10 mL of Tris buffer solution (10 mM, pH = 8.5), and 5 mg of dopamine hydrochloride was added. Under dark conditions at 300 rpm, the mixture was reacted for 3 h to obtain PDA surface-modified MSNs (DG@M-MSNs-PDA). Fifty milligrams of DG@M-MSNs-PDA was redispersed in 10 mL of sodium bicarbonate aqueous solution (pH = 7). Then, 1 mg of tris(2-carboxyethyl) phosphine and 5 mg of thiol-polyethylene glycol-folic acid (M = 2000) were added. Under dark conditions at 300 rpm, the mixture was reacted for 3 h to obtain folic acid-modified MSNs (DG@NPs).

Characterization

Transmission electron microscopy (TEM, FEI Talos F200x, USA) was utilized to characterize the morphology and structure of the nanoparticles at the microscopic level and to analyze the elemental distribution. The hysteresis loops of the nanoparticles were detected using a vibrating magnetometer (VSM, Lakeshore 7404, USA). A Fourier transform infrared (FTIR) spectrometer (6800 JASCO, Marseille, France) was used to analyze the characteristic absorption peaks of the nanoparticles. A laser particle size analyzer was used to detect the particle size, PDI and zeta potential of the nanoparticles. In addition, 3.0 T nuclear magnetic resonance instrument was used to verify the in vitro imaging performance of the nanoparticles.

Stability of and Drug Release from the Nanoparticles

To assess the stability of the DG@NPs, a 1 mg/mL dispersion of DG@NPs was prepared, and dynamic light scattering (DLS) measurements and polydispersity index (PDI) calculations were performed regularly (1, 7, 14, 21, and 28 days) (n=3).

To investigate the release efficiency of DOX in different pH environments, we added 5 mL (1 mg/mL) of DG@NPs to each of two dialysis bags with molecular weights ranging from 8.0 to 14 kDa, added the bags to PBS at pH 5.5 or 7.4, and stirred the solutions at 300 rpm. At 1, 2, 3, 4, 6, 8, 12, 24 and 48 h, we removed 3 mL of the solution and measured its absorbance at 233 nm. To maintain the original solution volume, we added 3 mL of fresh PBS simultaneously during each sampling.

The rates of drug loading and encapsulation were calculated using the following equations.

$$DLC\ (\%) = \frac{weight\ of\ the\ drug\ in\ NPs}{weight\ of\ NPs} \times 100\%$$

$$EE\ (\%)=\frac{weight\ of\ the\ drug\ in\ NPs}{weight\ of\ the\ drug\ in\ feed}\times 100\%$$

Biocompatibility

The cytotoxicity of the carriers was assessed with HPDE6C7 and SW1990 cells using the CCK-8 assay (6000 cells per well). Briefly, M-MSNs were then added at different concentrations (0, 5, 25, 50, 100, and 200 μg/mL) to the culture medium. After a 24 h incubation period, 10 μL of CCK-8 solution was added to the corresponding wells, and the cells were incubated for an additional 2 h. The absorbance of the resulting wells was then measured at a wavelength of 490 nm using a plate reader (SAFIRE2, TECAN, Menendorf, Switzerland). The in vivo biotoxicity of M-MSNs was determined using female BALB/c nude mice as model animals. All experiments were approved by the Animal Ethics Professional Committee of Qiqihar Medical University (QMU-AECC-2022-121). A high dose (50 mg/kg) of M-MSNs or saline was injected into the tail vein. Seven days later, the biochemical parameters of liver and kidney function was measured, the nude mice were sacrificed, and the organs were taken for histopathological examination.

In this study, a hemolytic assay method from the literature[34,35] was used to assess the hemocompatibility of the material. First, erythrocytes were centrifuged at 20 °C and 2000 rpm for 10 min and washed three times with saline to obtain a purified erythrocyte suspension. Then, 2 mL of a suspension containing 4% v/v erythrocytes was mixed with 2 mL of M-MSN dispersion. Additionally, H_2O and saline were added to erythrocyte suspensions as negative and positive controls, respectively. Next, all the mixes were incubated in a constant temperature incubator at 37 °C for 4 h and then centrifuged at 5000 rpm for 10 min. Finally, the absorbance values of the supernatants were measured at 576 nm.

The hemolysis percentage was calculated as follows.

$$Hemolysis\ (\%)=\frac{A_{sample}-A_{negative\ control}}{A_{positive\ control}-A_{negative\ control}}\times 100\%$$

Cellular Uptake

First, SW1990 cells in the logarithmic growth phase were inoculated in confocal dishes and incubated for 24 h. Then DG@NPs, DG@M-MSN-PDA and PBS were added to the cells, respectively, and the cells were co-cultured for 4 hours. A group of SW1990 cells was designed as a FA closed group, and FA was added to the closed group for a total incubation time of 4 h before the addition of DG@NPs. The cells were fixed in 4% paraformaldehyde for 20 min, followed by incubation with a DAPI solution for an additional 10 min. Finally, the cellular uptake of the DG@NPs was observed under a confocal microscope.

In vitro Cytotoxicity

Cells in a 96-well plate were coincubated with free DOX (1.125, 2.5, 6.125, 12.5, or 25 μg/mL), DOX@NPs or DG@NPs. The number of nanoparticles used had an amount of DOX equivalent to that in the free DOX group. After 24 h of incubation, 10 μL of CCK-8 reagent was added to each well for an additional one hour of incubation. Finally, the optical density at 450 nm was measured using a microplate reader. The following formula was used to calculate cell viability.

$$\text{Cell viability}\ (\%)=\frac{OD_{sample}-OD_{blank}}{OD_{contral}-OD_{blank}}\times 100\%$$

Cell Apoptosis

To investigate the impact of grafted FA nanoparticles on the apoptosis of pancreatic cancer cells, SW1990 cells were cultured in 6-well plates for 12 h. Subsequently, DG@M-MSNs-PDA and DG@NPs were introduced to each well for an additional 24 h of incubation. We also designed a FA intervention group where pancreatic cancer SW1990 cells were pre-treated with FA for 2h before DG@NPs were added and co-incubated with the cells. Pancreatic cancer SW1990 cells were collected, washed with PBS and resuspended in binding buffer, 5 μL of FITC-Annexin V solution was added and

mixed well, and then 5 μL of PI solution was added and incubated for 10 min under the influence of light, and apoptosis was detected by flow cytometry.

MR Imaging

To verify the MR imaging capability of the nanoparticles, solutions of different concentrations (0.05–0.5 mg/mL) were generated according to the Fe^{3+} content in the DG@NPs and placed in 5 mL centrifuge tubes for MR T_2 imaging.

To validate the in vivo imaging capability of the nanoparticles, T_2-weighted MRI was performed to verify the feasibility of using DG@NPs as in vivo MRI contrast agents. Tumor-bearing nude mice were anesthetized, and 100 μL of a DG@NPs dispersion was injected via the tail vein. Magnetic resonance images were acquired with a 3.0 T clinical magnetic resonance scanner at different times (1 h and 6 h) before and after injection to observe the changes in the T_2 signal in the tumor region of the nude mice.

In vivo Tumor Treatment

Tumor-bearing nude mice were divided into 4 groups (n = 5) and received injections of 100 μL of DG@NPs suspension via the tail vein every 2 days for a total of 15 days. During the treatment period, tumor volume and weight were measured once every 2 days to assess the rate of drug inhibition and toxic effects. At the end of the treatment cycle, the tumor and major organs were collected and weighed, and hematoxylin-eosin (H&E) staining and terminal deoxynucleotidyl transferase dUTP nick end labeling (TUNEL) were performed on the tumors and organs. The tumor volumes were calculated with the following formula.

$$Tumor\ volume\ \left(\mathrm{mm}^3\right)=\frac{1}{2}\ Length\times Width^2$$

Statistical Analysis

Data and statistical analysis were conducted using SPSS 20.0. Two-tailed Student's *t*-test was utilized for data with a normal distribution, while repeated-measures ANOVA was used to compare groups. The mean and standard deviation are used to express the results. A P value less than 0.05 was considered to indicate statistical significance.

Results and Discussion

Characterization

A drug delivery system utilizing DG@NPs is proposed herein. The synthesis process and mechanism of action are as follows (Scheme 1). First, Fe_3O_4 nanonuclei with good magnetic properties and monodispersity were obtained by thermal decomposition. Then, a mesoporous silica nanoparticle shell layer was wrapped around the Fe_3O_4 nanocore using the Stöber method to form a mesoporous material with high drug loading capacity and pH responsiveness. Next, the M-MSN surface was grafted with an amino group (M-MSN-NH_2) mediated by APTES to enhance the hydrophilicity and biocompatibility. Next, DOX was loaded into the mesopores through electrostatic interactions. Gox was added to the M-MSN-NH_2 surface through an amidation reaction. PDA was coated onto the surface of the M-MSNs to block the mesopores. Finally, folate-targeting polymer molecules were grafted onto the surface of PDA.

The TEM images of the Fe_3O_4 NPs, M-MSNs and DG@NPs are displayed in Figure 1A–C and Figure S1. Fe_3O_4 nanoparticles with a size of 11.16 ± 0.94 nm were prepared by the ferric oleate pyrolysis method,[36,37] and well-dispersed M-MSNs with an average size of 59.55 ± 3.36 nm were prepared by the conventional Stöber method.[35,38–40] As shown in Figure 1B–E, the DG@NPs were slightly larger (66.02 ± 3.6 nm) than the M-MSNs, which was due to the successful incorporation of PDA-PEG-FA on the M-MSN surface. The elemental content in the M-MSNs was then further analyzed using energy spectroscopy (Figure 1F), which allowed differentiation between the elements Fe, Si and O contained within the nanoparticles. Elemental mapping by high-angle annular dark field scanning (Figure 1G–K) provided more visual evidence of the core-shell structure and elemental distribution in the M-MSNs. From the X-ray diffraction data (Figure 2A), the characteristic diffraction peaks at

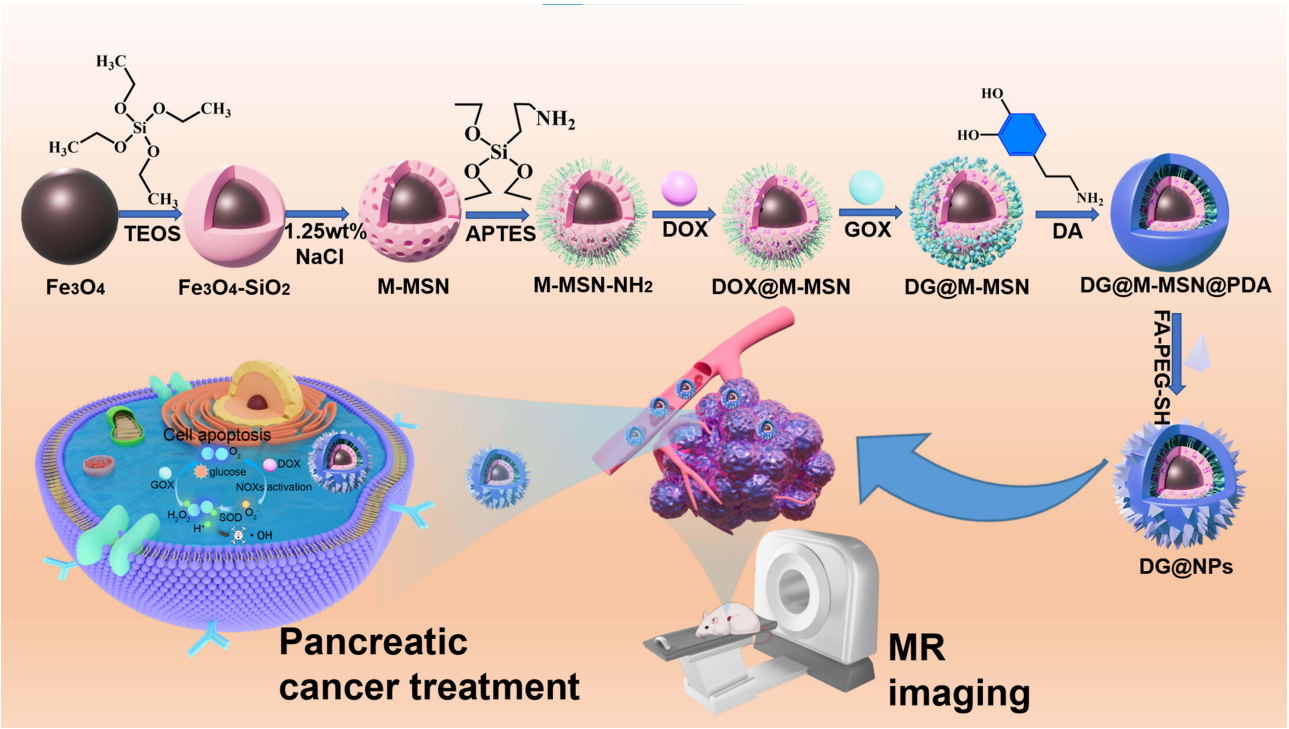

Scheme 1 Synthesis of DG@NPs and the mechanisms of diagnosis and treatment.

2θ = 30.1°, 35.5°, 43.1°, 53.4°, 57.0° and 62.6° were observed, corresponding to the (220), (311), (400), (422), (511) and (440) planes, respectively, which is consistent with the standard map of Fe_3O_4 nanoparticles (JCPDS. 72–2303); these data demonstrate the successful preparation of Fe_3O_4 with a crystalline structure. The characteristic peak of M-MSNs is between 15° and 30° and centered at 22°. This characteristic signal is attributed to amorphous silica. The DLS results showed that the average particle sizes of M-MSNs and DG@NPs were 134.9 nm and 191.7 nm, respectively. The DLS measurements are larger than the TEM results, which is attributed to the hydration layer around the particle surface in aqueous solution.[36,41,42] The particle size of the DG@NPs was larger than that of the M-MSNs, which might be due to the PDA coating. Moreover, The polydispersity index (PDI) of DG@NPs (0.31) was marginally lower than that of M-MSNs (0.36), implying that the PDA coating may have modestly improved the dispersion stability of DG@NPs (Figure 2B and C). According to the N_2 adsorption-desorption isotherms, the M-MSNs had a typical MCM-41 structure with a BET surface area of 653.19 m^2/g. From the BJH pore size distribution curves, it was observed that the average pore size in the M-MSNs was 5.00 nm and the total pore volume was 1.36 cm^3/g. For the DOX@M-MSNs, the above parameters were reduced to 609.65 m^2/g, 3.19 nm and 0.74 cm^3/g, and those for the DG@M-MSNs were reduced to 429.86 m^2/g, 2.86 nm and 0.30 cm^3/g, respectively (Figure 2D and E). This indicates the successful loading of Gox and DOX.

Based on the data in Figure 2F, the absorption peak at 575 cm^{-1} was ascribed to the Fe-O bond. Additionally, stretching vibrations at 1089 cm^{-1} and 781 cm^{-1} were observed, along with Si-O bending vibrations at 465 cm^{-1}. These findings suggest that the Fe_3O_4 nanoparticles were effectively coated with mesoporous SiO_2. Comparing Fe_3O_4-SiO_2 and M-MSNs, it is clear that the stretching vibrations at 2924 cm^{-1} and 2852 cm^{-1} and the bending vibration at 1469 cm^{-1} of C-H disappeared due to the complete removal of the template agent CTAB by NaCl/CH_3OH ion exchange. The appearance of an absorption peak at 1490 cm^{-1} originated from the C–N stretching vibration in M-MSN-NH_2.[30] In these spectra, the C-H stretching vibrations, NH_2 variable angle vibrations, and benzene ring C=C skeleton vibrations at 2930 cm^{-1}, 1651 cm^{-1}, and 1558 cm^{-1} were from the PDA material, This may be due to the PDA being encapsulated on the nanoparticle surface. In order to further prove the PDA coating, we carried out UV spectral analysis. It was found (Figure S2) that the characteristic UV

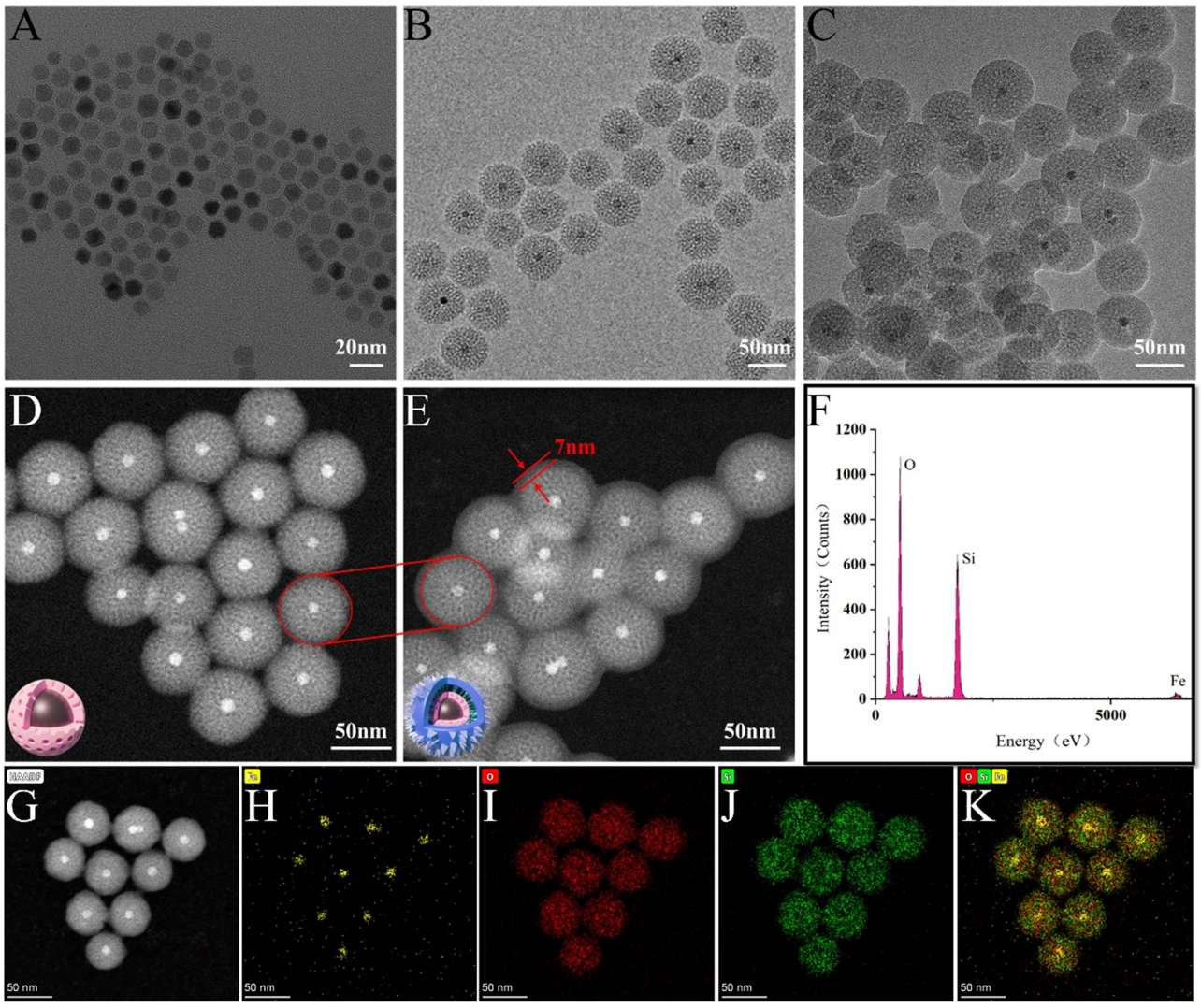

Figure 1 TEM images of Fe_3O_4 NPs (**A**), M-MSNs (**B**) and DG@NPs (**C**). TEM dark field images of M-MSNs (**D**) and DG@NPs (**E**). (**F**) EDS spectrum of M-MSNs; (**G**–**K**) M-MSN HAADF-STEM image and elemental mapping.

absorption peak of PDA appeared at 290 nm, which supported the successful coating of PDA. Additionally, the presence of the C=O stretching vibration peak at 1692 cm^{-1} indicated that the target ligand FA was present on the DG@NPs.[36] To confirm the successful preparation of DG@NPs, the magnetic saturation values of M-MSNs and DG@NPs were determined to be 1.31 and 1.03 emu/g (Figure 2G). This gradual decrease in magnetic saturation value is due to the successful encapsulation of PDA-PEG-FA. Zeta potential measurements (Figure 2I) showed that the M-MSN surface was negatively charged with a zeta potential of −26.23 mV. After APTES modification, the zeta potential shifted to 14.74 mV. The surfaces of DG@M-MSN-PDA and DG@NPs were slightly negatively charged with zeta potentials of −14.24 mV and −4.92 mV, respectively. These results suggest that APTES modification and SH-PEG-FA coupling can effectively alter the surface charge properties of M-MSNs. In summary, this evidence clearly and effectively demonstrated that folate-modified nanoparticles were successfully prepared.

Stability of the DG@NPs and in vitro Drug Release

To evaluate the stability of the synthesized DG@NPs, changes in particle size and PDI were observed and recorded in Figure 2J. The results indicate that the nanoparticles remained stable even after being stored in PBS

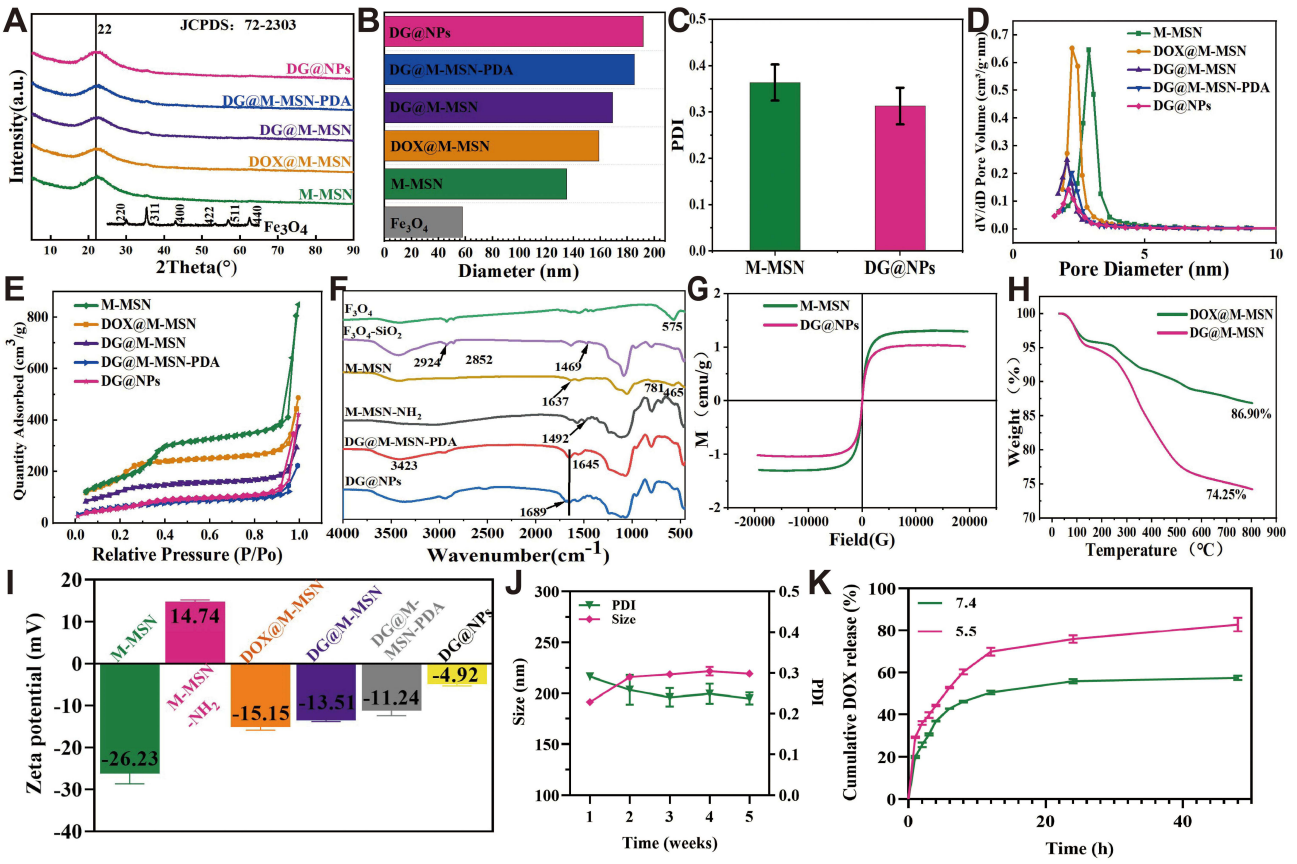

Figure 2 (**A**) XRD patterns of Fe_3O_4 and M-MSNs. (**B**) Size distribution profiles of M-MSNs and DG@NPs. (**C**) PDIs of M-MSNs and DG@NPs. (**D**) N_2 adsorption-desorption isotherms of M-MSNs, DOX@M-MSNs and DG@M-MSNs. (**E**) Pore size distributions of M-MSNs, DOX@M-MSNs and DG@M-MSNs. (**F**) FTIR spectra of various MSNs. (**G**) Hysteresis loops of M-MSNs and DG@NPs. (**H**) TGA curves corresponding to DOX@M-MSNs and DG@M-MSNs. (**I**) Zeta potential values of various MSNs (n=3). (**J**) Stability of the prepared DG@NPs. (**K**) Curve of in vitro DOX release from DG@NPs.

(pH 7.4) for 4 weeks. To determine the drug loading in DG@NPs, the mass loss between DOX@M-MSNs and DG@M-MSNs was analyzed using a thermogravimetric analyzer, which successfully determined a drug loading of 12.65% for Gox (as shown in Figure 2H, Figure S3). The DOX drug loading (7.61%) was calculated using the UV–vis adsorption peak intensity of DOX at 233 nm and the standard curve (Figure S4). The encapsulation rates (EE values) of the nanoparticles (38.05% for DOX and 42.17% for Gox) were calculated using the equation provided. In this study, the drug release from DG@NPs was examined using the dialysis method in PBS at different pH values. To simulate physiological conditions, the NPs were incubated at 37 °C with PBS at two pH values (7.4 and 5.5) representing normal blood and the lysosomal environment, respectively (Figure 2K). After 48 h of incubation, 58.65% of the DOX was released at neutral pH (7.4), while the DOX release increased to 82.78% at pH 5.5. This may be related to the existence of pH-dependent drug release characteristics of DG@NPs. Considering that the intracellular microenvironment is acidic, this pH-responsive drug release characteristic may contribute to the intracellular release of the drug.

Biocompatibility and Biotoxicity

Safety and nontoxicity are prerequisites for applied drug delivery systems. As shown in Figure 3A, when the concentration of M-MSNs reached 200 μg/mL, the survival rates of SW1990 cells and HPDE6C7 cells exceeded 80%. During the in vivo experiments, we monitored the body weights of the nude mice in both the carrier and control groups. As shown in Figure 3B, no weight loss was observed, and there were no deaths among the mice. The hemolysis ratio in all experimental groups was found to be less than 5%, meeting the hemolysis criteria for biological materials, as shown in Figure 3C. Moreover, the biochemical parameters of liver and kidney function and echocardiograms of tumor-bearing nude mice did not indicate any

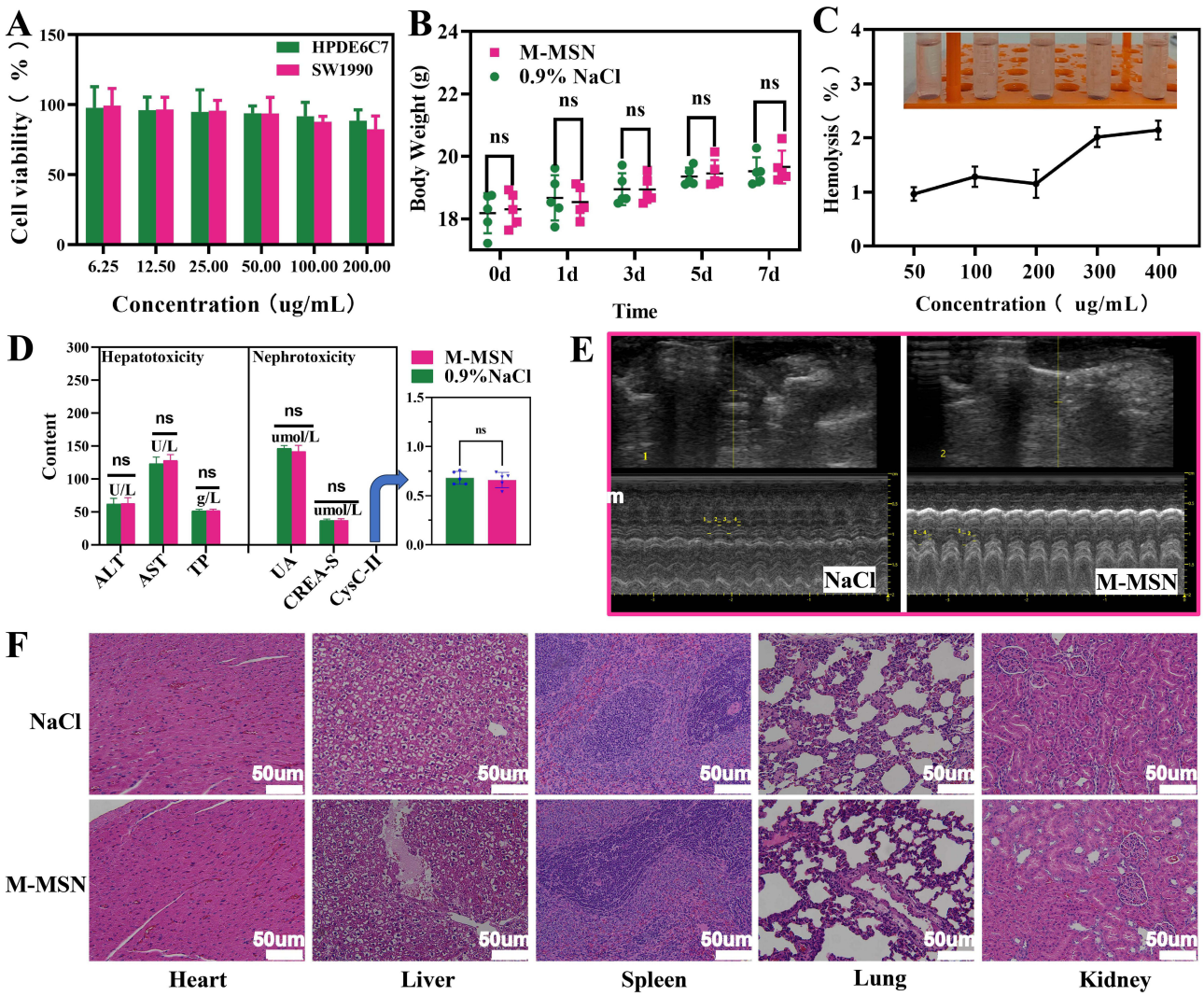

Figure 3 (**A**) Viability of SW1990 and HPDE6C7 cells after 24 h of treatment with M-MSNs. (**B**) the changes in nude mouse weight over one week (n = 5, ns: p>0.05). (**C**) The hemolytic efficiency of M-MSNs on erythrocytes. (**D**) Biochemical indicators of liver and kidney function (n = 5, ns: p>0.05). (**E**) Echocardiography of tumour-bearing nude mice. (**F**) H&E-stained images of organs dissected from the nude mice after treatment with 0.9% NaCl and M-MSNs (scale bars:50 μm).

organismal damage, as depicted in Figure 3D and E. Additionally, the H&E staining assay results revealed that the major organs of the M-MSN-treated nude mice did not exhibit any pathological changes, as shown in Figure 3F and Figure S5. These findings collectively suggest that M-MSNs are highly biocompatible.

Cellular Uptake

As shown in Figure 4, the intensity of the red fluorescence in cell after 4 h of incubation indicated successful uptake of the prepared nanoparticles by the tumor cells. The fluorescence intensity of the non-targeted group and the FA-intervention-targeted group was significantly lower than that of the targeted group. This result suggests the successful loading of FA, which effectively enhances the targeting of the nano drug-carrying platform.

In vitro Cytotoxicity

As shown in Figure 5A and B, with increasing DOX concentration, the abilities of the drugs to kill HPDE6C7 and SW1990 cells were enhanced. Among them, the cell mortality rate in the DG@NPs group was higher than that in the DOX@NPs group. This indicates that Gox amplified the antitumor effect of the chemotherapeutic drug DOX. In addition, we observed that there was no significant difference in cell mortality when HPDE6C7 cells were treated

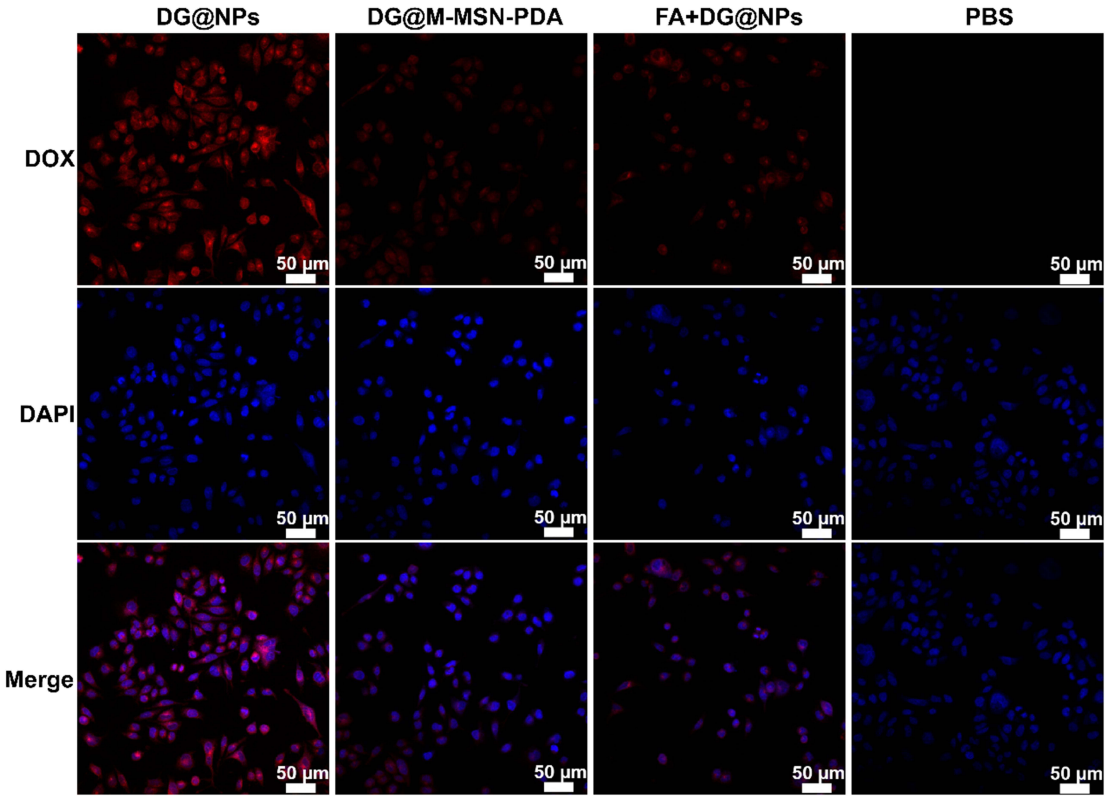

Figure 4 Confocal laser scanning microscopy images of SW1990 cells following incubation with DG@NPs, DG@M-MSN-PDA, FA+DG@NPs and PBS. Red and blue represent DOX and DAPI fluorescence, respectively (scale bar: 20 μm).

with free DOX and DOX@NPs. However, the mortality rate of SW1990 cells that highly express FR was significantly higher than that of HPDE6C7 cells at the same concentration. This indicates that the successful attachment of the targeting substance FA to the nanoparticles can enhance nanoparticle targeting and effectively promote the apoptosis of pancreatic cancer cells, thus enhancing the antitumor effect.

Cell Apoptosis

As shown in Figure 5C and D, the apoptotic rates of SW1990 cells treated with non-targeted (DG@M-MSN-PDA) and targeted group (DG@NPs) were (11.84 ± 0.42) % and (17.14 ± 0.47) %, respectively. The toxicity of targeted group was found to be significantly higher than that of non-targeted group, which was attributed to the active targeting properties of DG@NPs. The successful binding of the targeting substance FA to the nanoparticles enhanced nanoparticle targeting and improved the rate of pancreatic cancer cell apoptosis, which can strengthen the therapeutic effect of DOX.

MR Imaging Performance

The in vitro imaging performance of the DG@NPs is shown in Figure 6D and E. The T_2-weighted MR signal decreased with increasing Fe^{3+} ion concentration. The in vivo images of the DG@NPs are shown in Figure 6A–C, where the T_2 signal intensity at the tumor site was significantly reduced after nanoparticle injection. The results obtained indicate that the NPs prepared in this study have the potential to serve as contrast agents for MRI of tumors.

In vivo Tumor Treatment

Considering the desirable therapeutic effect and remarkable cytotoxicity observed in vitro, we initiated a study to evaluate its potential as an antitumor agent in vivo (Figure 7A). During the whole treatment experiment, the nude mice in the DG@NPs group did not show any deaths related to drug administration, and the changes in body weight were within the normal fluctuation range (Figure 7C), which was not statistically different from that of the control group, and it

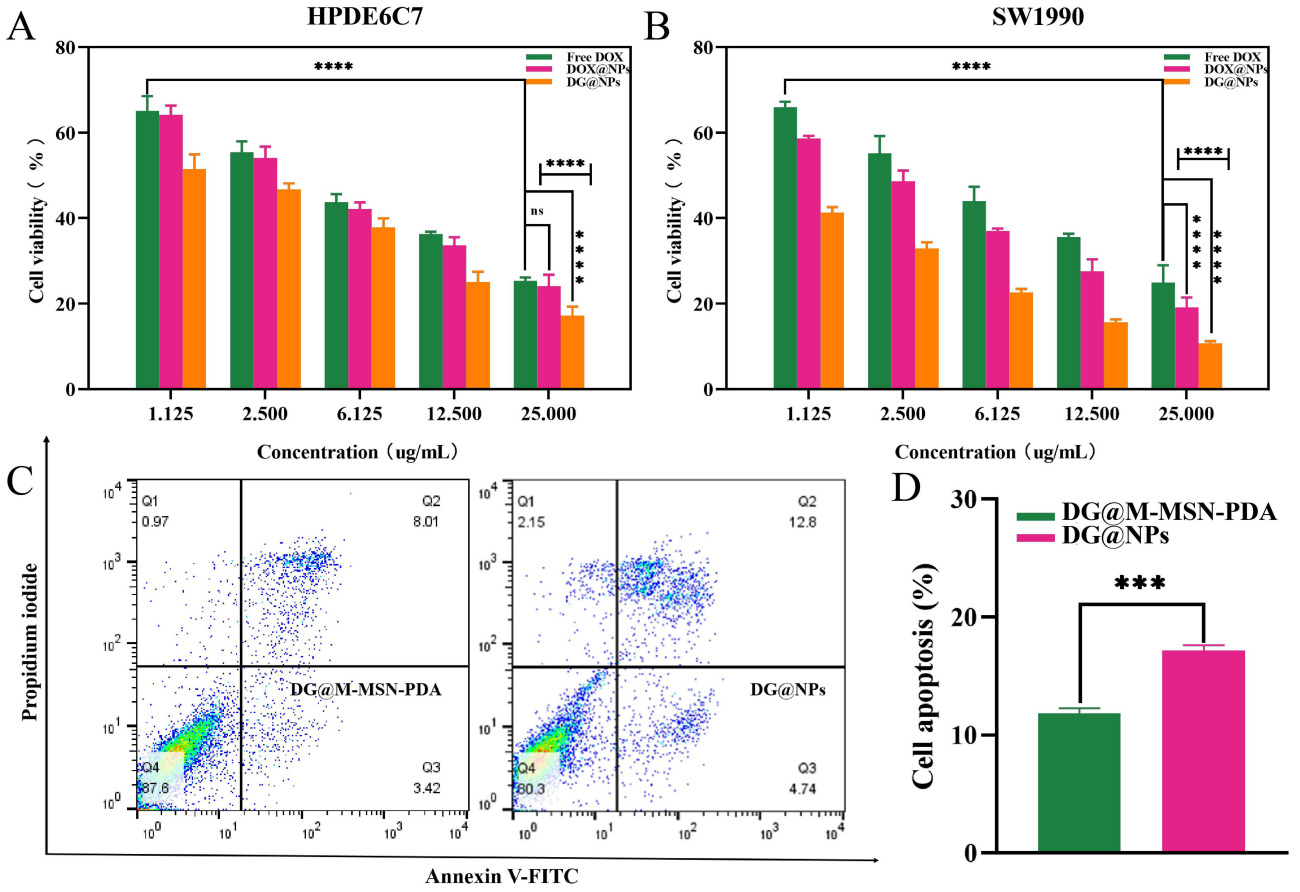

Figure 5 Relative viabilities of HPDE6C7 (**A**) and SW1990 (**B**) cells after incubation with free DOX, DOX@NPs and DG@NPs at different DOX concentrations. (**C**) Apoptosis of SW1990 cells induced by different pharmaceutical agents. (**D**) Bar graph summarizing the above total apoptosis rates (n=3; ****P < 0.0001, ***P < 0.001, ns: P >0.05).

was initially suggested that the drug-carrying nano-systems might be biocompatible with experimental nude mice within the set dosage range. At the end of the treatment, we performed HE staining examination of the organs of the nude mice in the DG@NPs group (Figure S5), and the results showed that no obvious damage was observed in the major organs. To further evaluate the biocompatibility of DG@NPs, we examined the liver and kidney function indexes (Figure S6) after one week of the drug-loaded nanoparticles' action, and the liver and kidney function indexes were also within the normal range. On the other hand, Figure 7D illustrates that the pace of tumor development in the PBS group showed no apparent inhibition. However, after 15 days of treatment, the pace of tumor development in the free DOX group and the DOX@NP group was somewhat inhibited, the tumor volume of the nude mice in the DG@NPs group was significantly reduced (Figure 7B), indicating that DG@NPs were the most effective treatment. The final tumor weights are presented in Figure 7E. The mean tumor weights were 0.29 g, 0.15 g, 0.22 g, and 0.11 g in the PBS, free DOX, DOX@NP, and DG@NPs groups, respectively, which corresponded with the trend of tumor volume growth. These findings confirmed that the DG@NPs had a more significant therapeutic effect than free DOX. Furthermore, Figure 7F shows that in the PBS group, the tumor tissue structure was normal, whereas in the free DOX, DOX@NPs, and DG@NPs groups, significantly increased areas of tumor necrosis were observed (as indicated by the arrows). In this study, it was found that the tumor tissue structure in the DG@NPs group was abnormal, with significantly more lamellar degenerative necrosis of the tumor cells than that in the PBS group and the free DOX group. This suggests that DG@NPs effectively kill cancer cells and can improve the efficacy of DOX when treating pancreatic cancer. The TUNEL assay further confirmed the pathological alteration observations and levels of the tumor cell apoptosis, indicating that DG@NPs have a strong toxic effect on pancreatic cancer cells and can induce apoptosis in vivo.

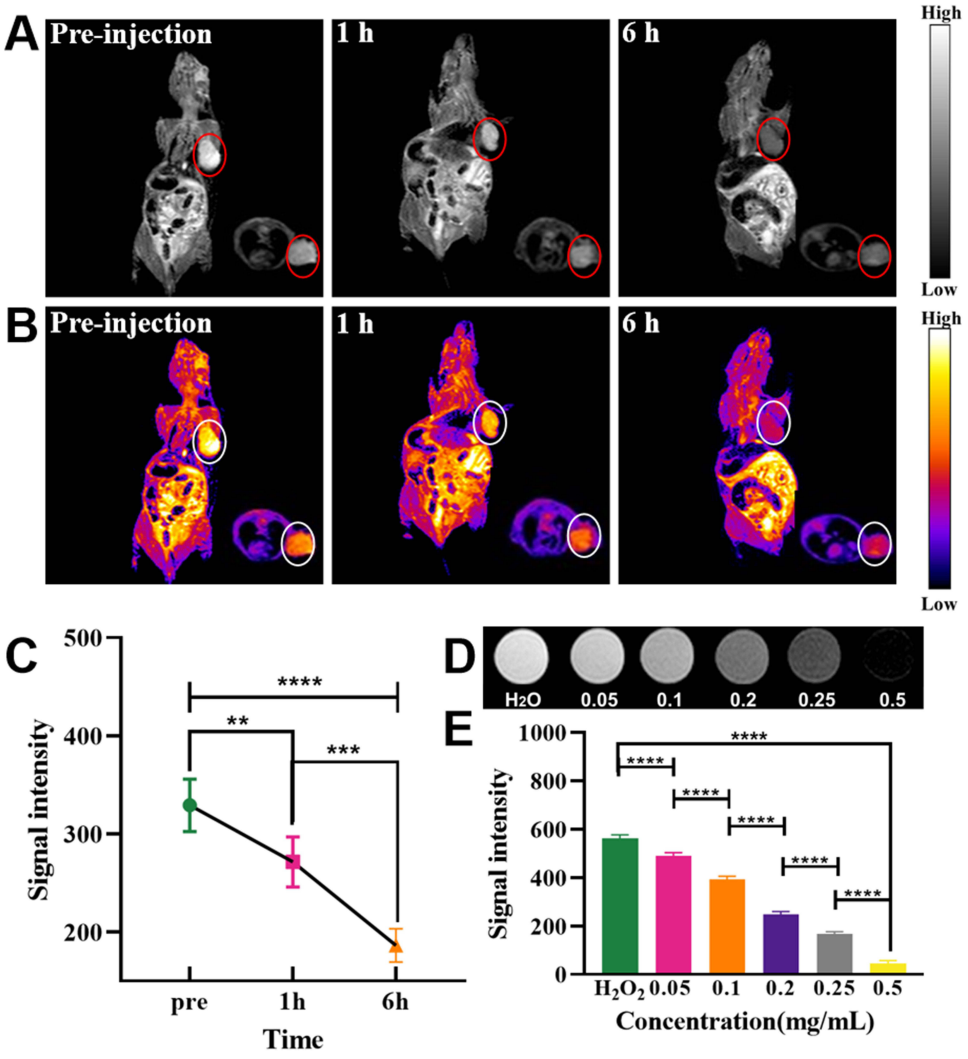

Figure 6 T_2-weighted magnetic resonance imaging (**A**), pseudo-color images (**B**) and signal intensity changes at tumour sites (**C**) at different times in vivo in tumor-bearing nude mice; in vitro magnetic resonance imaging (**D**) with different concentrations of DG@NPs and their signal intensity changes (**E**); (****P < 0.0001, ***P < 0.001, **P < 0.01).

Conclusion

In this study, pH-responsive DG@NPs were successfully developed to enhance the efficacy of DOX in the treatment of pancreatic cancer. The material was analyzed using various tools, including transmission electron microscopy, thermogravimetric analysis, nitrogen adsorption-desorption isotherms, and laser confocal microscopy. The results from the CCK-8 and H&E staining experiments indicated that the DG@NPs exhibited no apparent toxicity in both in vivo and in vitro, demonstrating their excellent biocompatibility. Studies performed in vivo and in vitro proved that the DG@NPs effectively inhibited pancreatic cancer cell growth and had good biosafety, making them a promising candidate for tumor diagnosis and treatment. Overall, DG@NPs provide a novel approach to detect and treat cancer.

Data Sharing Statement

The data and materials in the current study are available from the first author upon reasonable request.

Ethics Approval

This experiment was performed according to the protocol approved by the Animal Ethics Committee of Qiqihar Medical University (QMU-AECC-2022-121). In this study, we adhered to the ARRIVE guidelines and strictly followed the

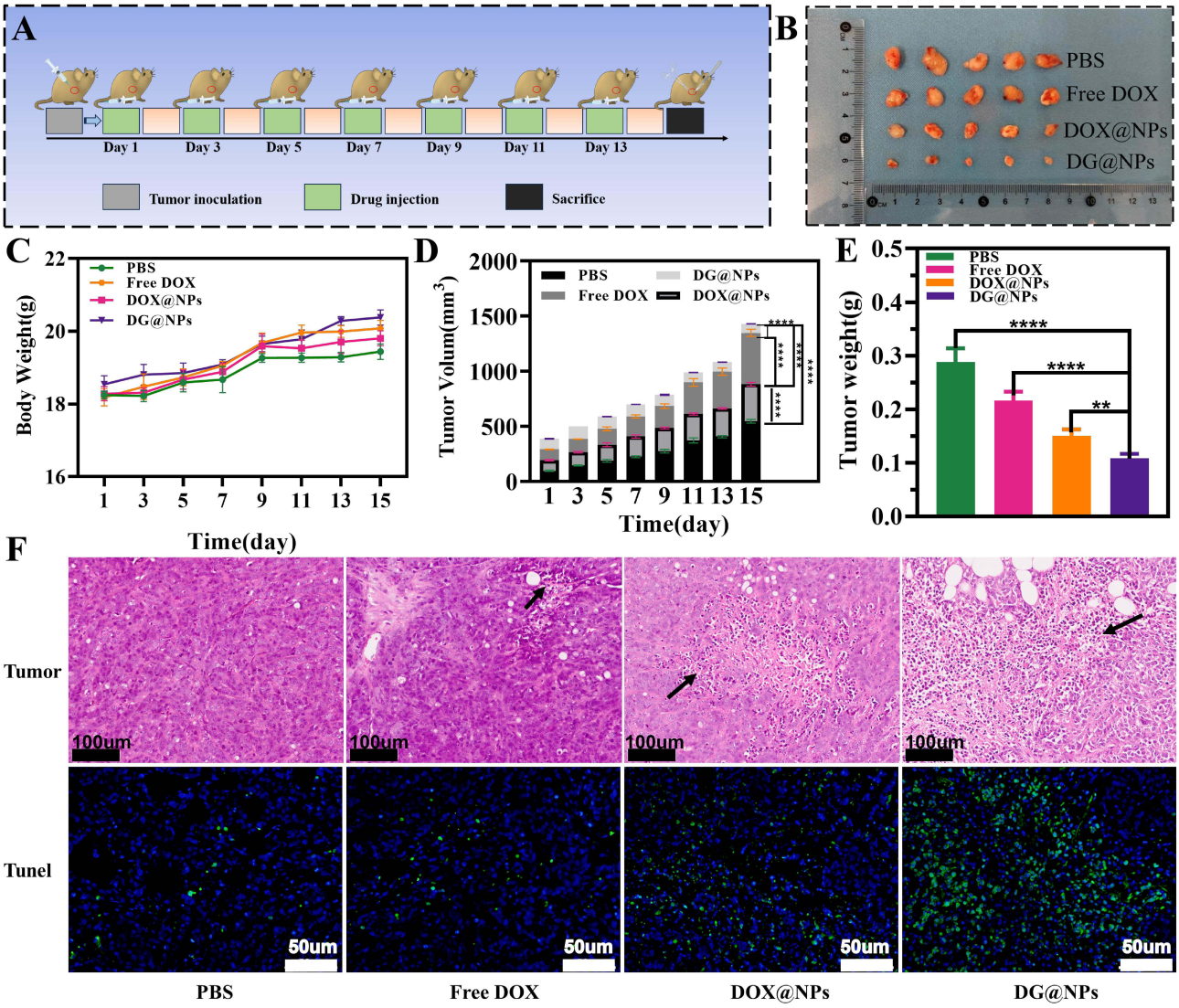

Figure 7 (**A**) Trial design for testing DOX/Gox combination efficacy on pancreatic cancer subcutaneous tumor model. (**B**) Tumor treatment effect graph. (**C**) Changes in the body weights of the nude mice in each group. (**D**) Tumor volume growth trends. (**E**) Final average tumor weights following 15 days of therapy. (**F**) H&E-stained tumor sections and TUNEL images of each group of tumor tissue (scale bar: 100μm, 50 μm; ****P < 0.0001 and **P < 0.01).

Regulations of the People's Republic of China on the Administration of Laboratory Animals and its guiding principles for animal experiments. Our approach fully respected the lives of laboratory animals and aimed to minimize their suffering.

Acknowledgments

We express our gratitude to Professor Guohua Li in the MRI aspect of the study.

Funding

This study was supported by grants from the Heilongjiang Provincial Health and Wellness Commission Fund Project (20210909010355) and Qiqihar Medical University Postgraduate Innovation Fund Project (No. QYYCX2022-01).

Disclosure

No potential conflict of interest was reported by the authors.

References

1. Siege RL, Miller KD, Fuchs HE, Jemal A. Cancer statistics, 2022. *CA*. 2022;72(1):7–33. doi:10.3322/caac.21708
2. Mizrahi JD, Surana R, Valle JW, Shroff RT. Pancreatic cancer. *Lancet*. 2020;395(10242):2008–2020. doi:10.1016/S0140-6736(20)30974-0
3. Shah VM, Sheppard BC, Sears RC, Alani AW. Hypoxia: friend or Foe for drug delivery in Pancreatic Cancer. *Cancer Lett*. 2020;492:63–70. doi:10.1016/j.canlet.2020.07.041
4. Springfeld C, Ferrone CR, Katz MHG, et al. Neoadjuvant therapy for pancreatic cancer. *Nat Rev Clin Oncol*. 2023;20(5):318–337. doi:10.1038/s41571-023-00746-1
5. Krissanaprasit A, Key CM, Pontula S, LaBean TH. Self-assembling nucleic acid nanostructures functionalized with aptamers. *Chem Rev*. 2021;121(22):13797–13868. doi:10.1021/acs.chemrev.0c01332
6. Liang C, Xu L, Song G, Liu Z. Emerging nanomedicine approaches fighting tumor metastasis: animal models, metastasis-targeted drug delivery, phototherapy, and immunotherapy. *Chem Soc Rev*. 2016;45:6250–6269. doi:10.1039/c6cs00458j
7. Wang ZY, Wu CC, Liu JR, et al. Aptamer-mediated hollow MnO2 for targeting the delivery of sorafenib. *Drug Deliv*. 2023;30:28–39. doi:10.1080/10717544.2022.2149897
8. Feng Y, Xie XX, Zhang HX, et al. Multistage-responsive nanovehicle to improve tumor penetration for dual-modality imaging-guided photodynamic-immunotherapy. *Biomaterials*. 2021;275:120990. doi:10.1016/j.biomaterials.2021.120990
9. Nel J, Elkhoury K, Velot É, et al. Functionalized liposomes for targeted breast cancer drug delivery. *Bioact Mater*. 2023;24:401–437. doi:10.1016/j.bioactmat.2022.12.027
10. Bao JF, Zu XY, Wang X, et al. Multifunctional Hf/Mn-TCPP metal-organic framework nanoparticles for triple-modality imaging-guided PTT/RT synergistic cancer therapy. *Int J Nanomed*. 2020;15:7687–7702. doi:10.2147/IJN.S267321
11. Raza F, Evans L, Motallebi M, et al. Liposome-based diagnostic and therapeutic applications for pancreatic cancer. *Acta Biomater*. 2023;157:1–23. doi:10.1016/j.actbio.2022.12.013
12. Xie Y, Hang Y, Wang Y, et al. Stromal modulation and treatment of metastatic pancreatic cancer with local intraperitoneal triple miRNA/siRNA nanotherapy. *ACS Nano*. 2020;14:255–271. doi:10.1021/acsnano.9b03978
13. Grafals-Ruiz N, Rios-Vicil CI, ozada-Delgado EL, et al. Brain targeted gold liposomes improve RNAi delivery for glioblastoma. *Int J Nanomed*. 2020;15:2809–2828. doi:10.2147/IJN.S241055
14. Kang H, Rho S, Stiles WR, et al. Size-dependent EPR effect of polymeric nanoparticles on tumor targeting. *Adv Healthc Mater*. 2020;9:e1901223. doi:10.1002/adhm.201901223
15. Cheng R, Jiang L, Gao H, et al. A pH-responsive cluster metal-organic framework nanoparticle for enhanced tumor accumulation and antitumor effect. *Adv Mater*. 2022;34:e2203915. doi:10.1002/adma.202203915
16. Hu JJ, Liu MD, Gao F, et al. Photo-controlled liquid metal nanoparticle-enzyme for starvation/photothermal therapy of tumor by win-win cooperation. *Biomaterials*. 2019;217:119303. doi:10.1016/j.biomaterials.2019.119303
17. Seth A, Gholami Derami H, Gupta P, et al. Polydopamine-mesoporous silica core-shell nanoparticles for combined photothermal immunotherapy. *ACS Appl Mater Interfaces*. 2020;12:42499–42510. doi:10.1021/acsami.0c10781
18. Li XD, Yu CG, Bao HY, Cheng SN, Huang J, Zhang ZJ. ROS-responsive janus Au/mesoporous silica core/shell nanoparticles for drug delivery and long-term CT imaging tracking of MSCs in pulmonary fibrosis treatment. *ACS Nano*. 2023;17:6387–6399. doi:10.1021/acsnano.2c11112
19. Sagir T, Isık S, Burgucu N, Tabakoglu O, Zaim M. Folic acid conjugated PAMAM-modified mesoporous silica-coated superparamagnetic iron oxide nanoparticles for potential cancer therapy. *J Colloid Interface Sci*. 2022;625:711–721. doi:10.1016/j.jcis.2022.06.069
20. Shosha NNH, Elmasry S, Moawad M, Ismail SH, Elsayed M. Invivo and invitro evaluation of antitumor effects of iron oxide and folate core shell-iron oxide nanoparticles. *Braz J Biol*. 2022;84:e253183. doi:10.1590/1519-6984.253183
21. Wang H, Mu QX, Revia R, et al. Iron oxide-carbon core-shell nanoparticles for dual-modal imaging-guided photothermal therapy. *J Control Release*. 2018;289:70–78. doi:10.1016/j.jconrel.2018.09.022
22. Thirumurugan S, Samuvel Muthiah K, Sakthivel R, et al. Chung, polydopamine-coated Cu-BTC nanowires for effective magnetic resonance imaging and photothermal therapy. *Pharmaceutics*. 2023;15:822. doi:10.3390/pharmaceutics15030822
23. Chen ZW, Sun YJ, Wang JW, Zhou X, Meng JS, Zhang XC. Dual-responsive triple-synergistic Fe-MOF for tumor theranostics. *ACS Nano*. 2023;17:9003–9013. doi:10.1021/acsnano.2c10310
24. Zhang T, Jiang ZQ, Xue T, et al. One-pot synthesis of hollow PDA@DOX nanoparticles for ultrasound imaging and chemo-thermal therapy in breast cancer. *Nanoscale*. 2019;11:21759–21766. doi:10.1039/c9nr05671h
25. Ding X, Bai SW, Liu FC, et al. NIR-II-triggered photothermal therapy with Au@PDA/PEG-PI for targeted downregulation of PSMA in prostate cancer. *Acta Biomater*. 2023;157:487–499. doi:10.1016/j.actbio.2022.12.017
26. Huo TT, Chen LL, Nie HF, et al. Mitochondrial dysfunction and antioxidation dyshomeostasis-enhanced tumor starvation synergistic chemotherapy achieved using a metal-organic framework-based nano-enzyme reactor. *ACS Appl Mater Interfaces*. 2022;14:3675–3684. doi:10.1021/acsami.1c18654
27. Hao SY, Zuo JJ, Huang HW, et al. Tumor microenvironment (TME)-modulating nanoreactor for multiply enhanced chemo dynamic therapy synergized with chemotherapy, starvation, and photothermal therapy. *J Mater Chem B*. 2023;11:1739–1748. doi:10.1039/d2tb02523j
28. Shen YM, Lv W, Yang HL, et al. FA-NBs-IR780: novel multifunctional nanobubbles as molecule-targeted ultrasound contrast agents for accurate diagnosis and photothermal therapy of cancer. *Cancer Lett*. 2019;455:14–25. doi:10.1016/j.canlet.2019.04.023
29. Cheng LX, Sang DM, Zhao FY, et al. Magnetic resonance/infrared dual-modal imaging-guided synergistic photothermal/photodynamic therapy nanoplatform based on Cu1.96S-Gd@FA for precision cancer theranostics. *J Colloid Interface Sci*. 2022;615:95–109. doi:10.1016/j.jcis.2022.01.099
30. Li B, Tan TF, Chu WW, et al. Co-delivery of paclitaxel (PTX) and docosahexaenoic acid (DHA) by targeting lipid nanoemulsions for cancer therapy. *Drug Deliv*. 2022;29:75–88. doi:10.1080/10717544.2021.2018523
31. Dong XW, Ye J, Wang YH, et al. Ultra-small and metabolizable near-infrared Au/Gd nanoclusters for targeted FL/MRI imaging and cancer theranostics. *Biosensors*. 2022;12:558. doi:10.3390/bios12080558
32. Wang J, Cen MP, Jing DN, et al. Gox-assisted synthesis of pillar [5] arene based supramolecular polymeric nanoparticles for targeted/synergistic chemo-chemodynamic cancer therapy. *J Nanobiotechnol*. 2022;20:33. doi:10.1186/s12951-021-01237-0

33. Fu LH, Hu YR, Qi C, et al. Biodegradable manganese-doped calcium phosphate nanotheranostics for traceable cascade reaction-enhanced anti-tumor therapy. *ACS Nano*. 2019;13:13985–13994. doi:10.1021/acsnano.9b05836
34. Zhang X, Wang YM, Zhao YB, et al. Sun, pH-responsive drug release and real-time fluorescence detection of porous silica nanoparticles. *Mater Sci Eng C Mater Biol Appl*. 2017;77:19–26. doi:10.1016/j.msec.2017.03.224
35. Li ZT, Guo J, Qi GQ, et al. Hao, pH-responsive drug delivery and imaging study of hybrid mesoporous silica nanoparticles. *Molecules*. 2022;27:6519. doi:10.3390/molecules27196519
36. Sun K, Gao ZG, Zhang Y, et al. Enhanced highly toxic reactive oxygen species levels from iron oxide core-shell mesoporous silica nanocarrier-mediated Fenton reactions for cancer therapy. *J Mater Chem B*. 2018;6:5876–5887. doi:10.1039/c8tb01731j
37. Kim MY, Ahn JP, Han SY, Lee NS, Jeong YG, Kim DK. Highly luminescent and anti-photobleaching core-shell structure of mesoporous silica and phosphatidylcholine modified superparamagnetic iron oxide nanoparticles. *Nanomaterials*. 2020;10:1312. doi:10.3390/nano10071312
38. Pérez-Garnes M, Morales V, Sanz R. Cytostatic and cytotoxic effects of hollow-shell mesoporous silica nanoparticles containing magnetic iron oxide. *Nanomaterials*. 2021;11:2455. doi:10.3390/nano11092455
39. Vaz-Ramos J, Cordeiro R, Castro MMCA, et al. Supercritically dried superparamagnetic mesoporous silica nanoparticles for cancer theranostics. *Mater Sci Eng C Mater Biol Appl*. 2020;115:111124. doi:10.1016/j.msec.2020.111124
40. Cheng W, Nie JP, Xu L, et al. pH-sensitive delivery vehicle based on folic acid-conjugated polydopamine-modified mesoporous silica nanoparticles for targeted cancer therapy. *ACS Appl Mater Interfaces*. 2017;9:18462–18473. doi:10.1021/acsami.7b02457
41. Wang S, Qi G, Zhang Z, et al. cRGD-conjugated GdIO nanoclusters for the theranostics of pancreatic cancer through the combination of T1-T2 dual-modal MRI and DTX delivery. *Molecules*. 2023;28:6134. doi:10.3390/molecules28166134
42. Guo X, Wu Z, Li W, et al. Appropriate size of magnetic nanoparticles for various bioapplications in cancer diagnostics and therapy. *ACS Appl Mater Interfaces*. 2016;8:3092–3106. doi:10.1021/acsami.5b10352